Title

Design and implementation of a multifrequency near-infrared diffuse optical tomography system

Permalink

https://escholarship.org/uc/item/1k85n724

Journal

Journal of Biomedical Optics, 11(1)

ISSN

1083-3668

Authors

Gulsen, Gultekin
Xiong, Bin
Birgul, Ozlem
et al.

Publication Date

2006

Peer reviewed

Design and implementation of a multifrequency near-infrared diffuse optical tomography system

Gultekin Gulsen
Bin Xiong
Ozlem Birgul
Orhan Nalcioglu
University of California
Tu and Yuen Center for Functional Onco-Imaging
Irvine, California 92697
E-mail: ggulsen@uci.edu

Abstract. The design and implementation of a multifrequency and multispectral diffuse optical tomography system is described. Four wavelengths are utilized: 665, 785, 808, and 830 nm. The system is based on a network analyzer, which provides rf modulation signals for the laser diodes, as well as measures the amplitude and the phase of the detected signals. Six different modulation frequencies ranging from 110 to 280 MHz are used. The details of instrumentation, calibration, data acquisition, and performance of the system are given. A finite element algorithm is used to solve the diffusion equation, and an inverse solver based on this forward solver is implemented to calculate the absorption and scattering maps from the acquired data. Data acquisition for one wavelength is completed in less than 2.5 min for a single modulation frequency. The measurement repeatability is 0.5% in ac intensity and 0.2 deg in phase. The performance of the system is evaluated with phantom studies. A multifrequency reconstruction algorithm is used, in which a single absorption and scattering image pair is obtained using the whole dataset obtained at different modulation frequencies. It is shown that the multifrequency reconstruction approach provides superior image quality compared to the single frequency counterpart. © *2006 Society of Photo-Optical Instrumentation Engineers.* [DOI: 10.1117/1.2161199]

Keywords: multifrequency; optical tomography; network analyzer.

Paper 05088R received Apr. 4, 2005; revised manuscript received Jul. 26, 2005; accepted for publication Aug. 29, 2005; published online Jan. 24, 2006.

1 Introduction

In recent years, near-infrared (NIR) imaging has been an emerging technique for noninvasive biomedical imaging.[1–5] Diffuse optical tomography (DOT) provides absorption and scattering maps of tissue by measurements through tissue at several projections with a diffusion-based model. Using multiwavelength measurements, the absorption and scattering maps for different wavelengths can be obtained. Multiwavelength measurements allow evaluation of the hemoglobin concentration, oxygen saturation, fat, and water content. Hemoglobin concentration has been used as a tool for functional imaging of human cerebral activity and cancer detection based on the associated vasculature.[6–11] Although continuous wave imaging is the most robust and economic choice, the average photon path traveled can be derived from the time-resolved and frequency-domain measurements in addition to the measured optical flux. These additional data provide uniqueness to the solution of recovering both coefficients simultaneously, and allow the separation of absorption and scattering.[12] Frequency-domain systems require less expensive instrumentation compared to time-resolved systems, and have been successfully applied for imaging.[13–16] In general, a single modulation frequency is used due to the complexity of

the instrumentation and time limitations. As the modulation frequency increases, the phase shift difference between normal and tumor tissue increases; however, the sensitivity and accuracy of the detection system decreases.[12] Therefore, most of the DOT devices utilize modulation frequencies around 100 MHz and the dedicated wavelengths at which the information content is maximal.

We present a DOT system utilizing multiple discrete frequencies (MF-DOT) to explore the benefits of combining multifrequency information with multispectral information. A finite element method (FEM)-based reconstruction algorithm based on a diffusion equation is used to generate tomographic images of absorption and scattering. A Newton-type algorithm is used to obtain the solution that provides minimum error between the measured data and estimated measurements from the FEM forward solver. Fan-beam detection geometry was used and a fiber optical interface was constructed. Solid phantoms were used to evaluate the performance of the system.

2 Methods

The design and construction of the frequency-domain near-infrared detection system and the details of data acquisition and analysis are described in this section.

Address all correspondence to Gultekin Gulsen, Center for Functional Onco-Imaging, UC Irvine, Irvine Hall - Rm # 164, Irvine, CA 92697. Tel: 949–82406557. Fax: 949–824–3481. E-mail: ggulsen@uci.edu
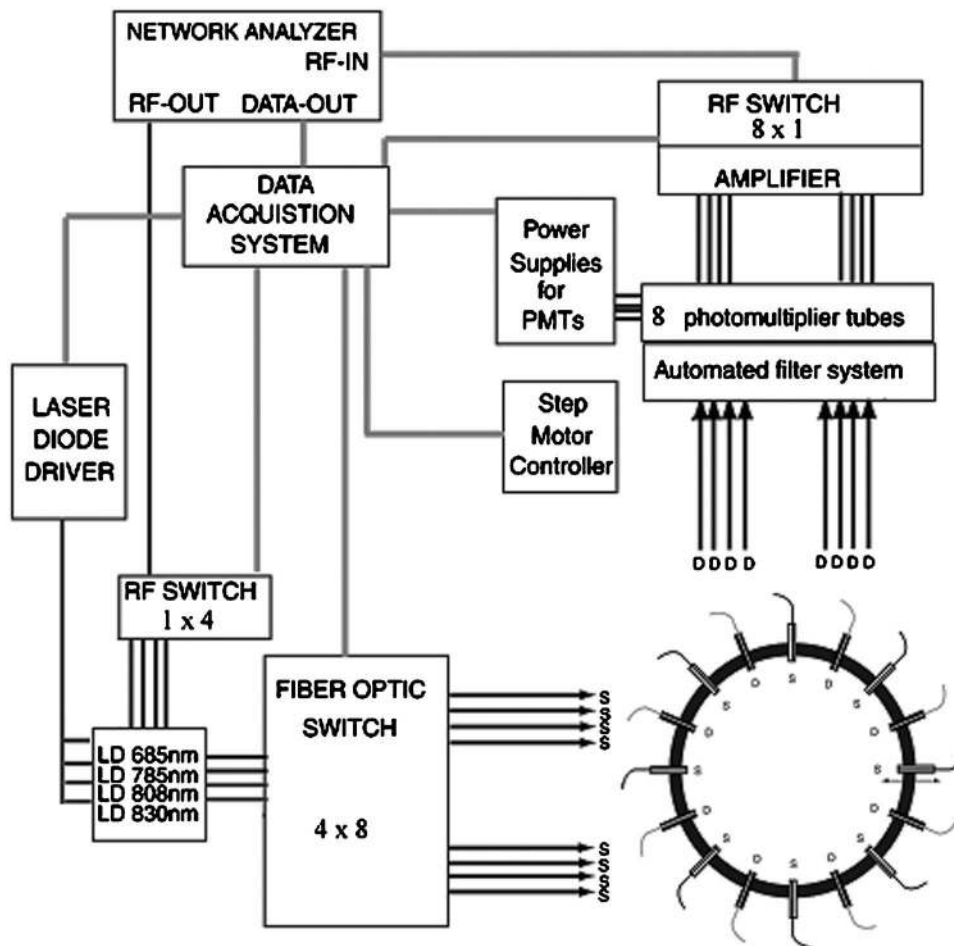
Fig. 1 The schematic diagram of the multifrequency DOT setup.

2.1 Instrumentation

The MF-DOT system is based on a network analyzer (Agilent Technologies, Palo Alto, California). The network analyzer not only measures the amplitude and the phase of the detected signals, but also provides the rf signal to modulate the amplitude of the laser diode sources. Figure 1 shows the schematic of the DOT system. The system employs four different wavelengths: 665 nm (50 mW, Intelite, Genoa, Nevada), 785 nm (75 mW, Thorlabs, Newton, New Jersey), 800 nm (150 mW, Intelite, Genoa, Nevada), and 830 nm (100 mW, Intelite, Genoa, Nevada). The laser diodes are driven by a dc current source (ILX Lightwave, Bozeman, Montana). A bias-T allows the modulation of the lasers with the modulation signal generated by the network analyzer at the selected frequencies. A four-way power splitter (Mini-Circuits, Brooklyn, New York) is used to divide the rf signal into four, and a separate amplifier (Mini-Circuits, Brooklyn, New York) is used to amplify each signal prior feeding to the bias-Ts. A temperature-controlled laser diode base (Thorlabs, Newton, New Jersey) is used for each laser diode. A fiber optic switch (DICon Fiberoptic, Richmond, California) is used to multiplex the laser diode outputs through the source fibers. It has 1.2-dB loss, less than ±0.03-dB repeatability, maximum −80-dB cross talk, and approximately 300-ms switching time. The source fibers connected to the output of the fiber optic switch lead to

the fiber optic interface and transfer the lasers' outputs to the sample. The four laser mounts that hold the lasers are placed in a metal box.

Photomultiplier tubes (PMT) are chosen as detectors able to measure low-level signals in fan-beam geometry. Eight PMTs (R7400U-20 Hamamatsu, Japan) are used, one for each detection site. The R7400U series is a subminiature photomultiplier tube 16 mm in diameter and 12 mm in length. This PMT has an eight-stage electron multiplier composed of metal channel dynodes and features excellent response time. It has a rise time of 0.78 ns and f_{3DB} around 200 MHz. Although its performance is degraded with increasing frequency, it has a better frequency response compared to other PMTs due to its faster rise and fall times. Typical spectral response of R7400U-20 covers the 300- to 900-nm range with 50-mA/W cathode radiant sensitivity at 800 nm. A compact on-board-type high-voltage power supply (Hamamatsu, Japan) is used for each PMT. The gain of PMTs can be adjusted separately by applying voltages between 1 to 4 V to the control input of these high-voltage power supplies. These eight control voltages are supplied by a computer via a DAC card (National Instruments, Austin, Texas). The gain of each PMT can be adjusted individually and is determined at the beginning of an experiment. With the help of a photodiode (Hamamatsu, Japan) mounted on the rotation stage in the detection unit, the

Fig. 2 The detection unit. The PMTs and the detector fibers were arranged in a circular geometry and fixed. A rotation stage was used to change the positions of the filters.

Fig. 3 The fiber optic adaptive interface, fiber optic probes, and the solid phantom with a hole.

approximate intensity collected by each fiber can be monitored. For each source position, the photodiode is positioned right under each detector fiber sequentially, and the photodiode output is measured by a transimpedance amplifier (Terahertz Technologies, Oriskany, New York). The output of the transimpedance amplifier is monitored and recorded by the computer with a general purpose DAQ card (National Instruments, Austin, Texas). Based on these approximate values, the initial gain setting of each individual PMT is determined. During an imaging session, the gains of the PMTs are kept constant. The outputs of the PMTs are multiplexed by an 8×1 rf switch (Hitite, Chelmsford, Massachusetts) and amplified by a 65-dB amplifier (Sonoma Instruments, Sonoma, California). The rf switch uses a GaAs switch and has 0.8-dB insertion loss and more than 55-dB isolation at 100 MHz.

The detectors nearest to the source receive orders of magnitude more incident light than those that are the farthest due to the detection geometry. Thus, either the light level or the gain of the PMT must be adjusted because of the limited dynamic range of the PMT. A filter wheel is inserted between the PMTs and fibers in the coupling system to adjust the light level. The PMTs and the detector fibers are arranged in a circular geometry and placed in a detection unit. A rotation stage with high repeatability is used to change the positions of the filters and keep them fixed relative to the source, as shown in Fig. 2. Therefore, the extensive dynamic range of the intensity measured from the sample is reduced to the dynamic range of the PMTs. The positions of the PMTs and the detector fibers are kept fixed and do not involve any mechanical motion. The gain of each PMT can even be set to the same value with the adjustment of the filters. This made the calibration procedure easier and reduced any error potentially inherent in other types of calibration techniques. Keeping the PMT's bias voltage constant during the experiment decreases the voltage hysteresis, while the neutral density filters limit the dynamic range of the light detected by the PMT, thus reducing the light hysteresis.

The PMTs, their high-voltage power supplies, the rf switch, the filter wheel, and the rotation stage are all placed in a shielded aluminum box. This detection unit has three levels, as shown in Fig. 2. The upper level holds the detector fibers and the high-voltage power supplies. The middle level is the aluminum filter wheel mounted on a high-precision rotation stage (Phytron, Waltham, Massachusetts). The filter wheel is 20 in. in diameter and can accommodate up to 32 filter hold-

ers. The rotation stage is driven by a step motor power drive (National Instruments, Austin, Texas) and a motion controller card (National Instruments, Austin, Texas). The bottom level accommodates the PMT holders, the rf switch, and the amplifier unit. All parts of this detection unit were precision machined. The power supply lines for the circuits and the rotation stage, the control voltages for the high-voltage power supplies, and the rf switch are filtered by feed-through filters located on one side of the aluminum box.

2.2 Fiber Optic Interface

Optical fibers are used both to conduct light from the sources to the tissue and to transfer the collected light from tissue to detectors. 62.5-μm core diameter gradient-index fibers are used as the source fibers, while 1.1-mm core diameter step-index fibers are used as the detector fibers. An adaptive interface was constructed to hold the sample and position the tips of source and detector fibers around the full circumference of the sample (Fig. 3). It consists of eight-source and eight-detector fiber probes with radically adjustable holders. Fiber probes were machined in a cylindrical form with a center hole that contains the fiber. Custom-made glass ferrules were used to fix and polish the tips of the fibers with the help of a polishing machine (Ultratec, Santa Ana, California). After polishing, each ferrule was positioned at the end of each probe and glued. A pair of molybdenum disulfide (MDS) filled nylon bearings (McMaster-Carr, Atlanta, Georgia) hold and guide each probe accurately in radial position. A compression spring is used for each probe to provide the required pressure to hold the fiber on the sample surface. The design allows having the same pressure level at each probe position (Fig. 4). The sample is placed at the center of the fiber optic interface, and the fiber probes are radially adjusted until they are in contact with the sample.

2.3 Data Acquisition

A PC controls and synchronizes all of the equipment. Lab Windows CVI (National Instruments, Austin, Texas) is utilized for programming. The network analyzer measures the amplitude and the phase information from each detector. It provides heterodyne detection, and therefore gives a higher
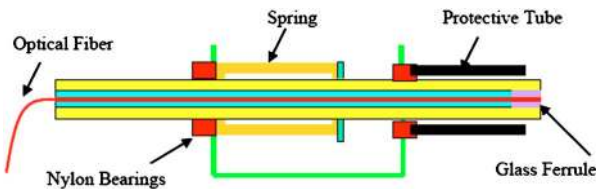
Fig. 4 The spring-loaded fiber optic probe.

accuracy in phase detection by down-converting a received signal to an intermediate frequency (IF) that is much lower than the signal itself. In this study, the IF bandwidth of the network analyzer is set to 15 Hz. The dynamic amplitude error contribution is 0.1 dBm between +10 and −50 dBm, while the dynamic phase error contribution is around 0.5 deg in the same range. The phase and amplitude of each PMT signal is acquired for approximately 2.5 s, averaged, and transferred to the computer via a GPIB card (National Instruments, Austin, Texas). For each of the eight source locations, measurements are done for eight detector locations, giving 64 measurements for each wavelength. The rotation stage accomplishes 45-deg movements required for the filter positioning in less than 300 ms. Hence, this motion can be accomplished in parallel with the fiber optic switching and no extra time is required. The measurement time for one wavelength, including monitoring time for each PMT signal and 300-ms switching time for source multiplexing, is around 2.5 min.

2.4 Phantom Design

Two 63-mm-diam solid phantoms simulating tissue optical properties were constructed using the method described by Firbank, Oda, and Delpy.[17] The optical properties of the phantoms were $\mu a=0.0132$ mm^{-1} and $\mu s'=0.86$ mm^{-1} at 785 nm. One of them was used for calibration purposes (homogeneous case), and a 15-mm hole was drilled on the other one to simulate different embedded objects (heterogeneous case). The hole was filled with varying concentrations of Intralipid (10%, F.K. Clayton, Clayton, North Carolina) and Indian ink (Winsor and Newton, England) in water to test the performance of the system. A separate solid shell was prepared to characterize the optical properties of the Intralipid and the Indian ink. Different concentrations of Intralipid and Indian ink in water were placed in the solid shell phantom and measurements were acquired. The absorption coefficient of the solid phantom was higher than the breast tissue to evaluate the sensitivity of the system. Due to high absorption, the measured signals were around subpicowatt range when the separation between the source-detector probes was maximum, which was nearly the minimum detectable signal range, especially at high frequencies.

2.5 Calibration

Calibration is the pivotal part of the data acquisition due to the variation in characteristics of each PMT, optical fiber, and neutral density filters. An accurate calibration is achieved in three steps: filter calibration, detector calibration, and homogeneous phantom calibration.

2.5.1 Filter calibration

As explained in Sec. 2.1 on instrumentation, the filters are used to reduce the extensive dynamic range of the measured intensities. They are placed on a filter wheel, and their positions between PMTs and fibers in the coupling system are adjusted by a rotation stage. Not only the optical densities of two similar (manufacturer specified) filters would be different, but also the attenuation could be different throughout the area of the filter, depending on the position of the incident beam. The optical densities (ODs) of the filters are also wavelength dependent. Therefore, the attenuation of the filters have to be measured individually as a function of the position and wavelength. For a certain wavelength, each filter is positioned between each PMT-fiber couple, hence the OD of the filter is measured for all possible positions. There are no filters for the two minimum signals detected at the farthest two positions with respect to a specific source. This reduced the number of filters to six, and a total of 48 measurements are done corresponding to eight different positions. The filter OD values are recorded to a calibration file to calibrate all the data obtained from a measurement set. As an example, the OD values for the six filters at a specific filter wheel position are 3.22, 1.32, 0.81, 0.82, 1.32, and 3.18 at 785 nm. The variation in the OD values is around 0.03 for different possible positions. The filter calibration had been repeated a number of times on different days and no significant change in the OD values were observed. Therefore, this calibration step is repeated less frequently after major changes are made in the detection unit or if the system is moved. The other two calibration steps, detector and homogeneous phantom calibrations, are repeated after each experiment to minimize the errors arising from the calibration procedure.

2.5.2 Detector calibration

The detector fiber-PMT combination and the performance of the corresponding rf switch port will determine the signal strength measured from detection sites. Each PMT will have different amplitude and phase response to the same optical signal. Although the detector fibers were polished carefully and cut to the same length, they have different light collection efficiency and introduce different phase lag. In addition to that, each channel of the rf switch has a different offset. To take all these effects into account, a source is placed at the center of the phantom and measurements are obtained at each detector site.[15,18,19] Each detection fiber is exposed to the same optical signal, and the differences in the amplitude and phase measurements are recorded as calibration factors. To eliminate the effect of possible inheterogeneity in the phantom, the calibration measurements are repeated three times and the phantom is rotated 45 deg before each measurement. Table 1 shows a set of detector calibration measurements for the modulation frequency of 110 MHz. The PMT bias voltage was kept at 900 V for these measurements.

2.5.3 Homogeneous phantom calibration

A homogeneous phantom is used for this calibration procedure. The amplitude and the phase of each PMT output signal are recorded for all eight sources. After the application of the filter and detector calibrations, the data are averaged over all sources and a homogeneous fit is performed. The resulting fit

Table 1 A set of detector calibration measurements for the modulation frequency of 110 MHz. The PMT bias voltage was kept at 900 V for these measurements.

	Amplitude (dBm)	Phase (Degrees)
PMT1	−29.40	38.92
PMT2	−30.27	−62.57
PMT3	−24.23	−51.06
PMT4	−34.92	−37.04
PMT5	−31.22	−23.90
PMT6	−29.26	−33.55
PMT7	−30.12	−31.89
PMT8	−25.63	−14.35

is used to determine the optical properties of the phantom, and the differences between the fit and 64 individual measurements are recorded as a final calibration factor. This calibration is performed to account for the fiber differences in transmission and alignment and the discretization errors due to data/model mismatch.[15,20]

2.6 Data Analysis

The diffusion approximation to the transport equation is given as

$$\frac{\partial \Phi(r,t)}{\partial t} - \nabla \cdot c(r)\kappa(r)\nabla\Phi(r,t) + c(r)\mu_a(r)\Phi(r,t) = q_o(r,t),$$

$$\forall r \in \Omega,$$

where $\Phi(r,t)$ is the photon density, $\mu_a(r)$ is the absorption coefficient, $\kappa(r) = \{3[\mu_a(r)+\mu_s(r)]\}^{-1}$ is the diffusion coefficient, $\mu_s'(r)$ is the reduced scattering coefficient, $c(r) = c_o/n$ is the speed of light, and n is the refractive index. The Robin boundary condition is

$$\Phi(\xi) + \hat{a}_n \cdot 2\kappa A \nabla \Phi(\xi) = 0, \quad \forall \xi \in \partial\Omega,$$

where $\hat{a}_n$ is the outward normal to the boundary $\partial\Omega$ at ξ.

The finite element method (FEM) is used for the solution of the forward problem defined by the diffusion equation. A FEM mesh of 1761 nodes and 3264 first-order triangular elements is constructed with denser element distribution underneath the boundary. The source is place at a location $1/\mu_s'$ below the surface. A coarser mesh with 289 nodes and 512 elements is used for the solution of the inverse problem. For the solution of the inverse problem, the relation between the measurements and the unknown absorption and scattering coefficients are linearized around an initial as:

$$J\Delta\mu = \phi_m - \phi_c,$$

where $\Delta\mu$ is the change in μ_a and μ_s with respect to initial values, J is the Jacobian, ϕ_m is the measurement, and ϕ_c is

the calculated values for the initial distribution.[21] Multiplying both sides of the equation by J^T and incorporating the Tikhonov regularization parameter λ, the equation to be solved becomes:

$$(J^T J + \lambda I)\Delta\mu = J^T(\phi_m - \phi_c).$$

The optimum regularization parameter is found using the one-curve method.[22] Since the relation between optical coefficients and measurements is nonlinear, the linear approximation is iterated using the updated coefficients as initial. The iterations are stopped when the changes in optical coefficients in consecutive iterations are below a threshold. The data are split into amplitude and phase components during reconstruction. Due to the difference in the dynamic range of the measurements, it is not possible to use them in the Jacobian directly; therefore, we used ten times the logarithm of the magnitude measurements. Another scaling is done to account for the range difference in scattering and absorption coefficients. The scaling factor is determined as the ratio of the mean initial scattering distribution to the mean absorption distribution. Calibration and preprocessing of the data are the necessary steps before reconstruction and are very critical in determining the quality of images. We first apply center and filter calibration to the measured data as discussed in the previous sections. Later, we apply homogeneous phantom calibration, hence we donot need to use any other weighting for the differences between the measurement and forward problem. Another important step in the reconstruction is the determination of the initial distribution in the iterative solution. We apply homogeneous fitting to the measured data and use fitted values as the initial distribution. The mismatch in the refractive index due to the liquid inclusion in the solid phantom has been modeled in the FEM forward solver.

First, the absorption and scattering images were reconstructed at discrete frequencies separately. Later, a multifrequency approach was used, in which a single absorption and scattering image pair was obtained using the whole dataset obtained at different modulation frequencies. In this approach, the sensitivity information coming from each frequency coupled together to form a single Jacobian. One of the advantages of the new form of the Jacobian is that it makes the reconstruction more immune to noise than the single frequency counterpart.

3 Results

3.1 System Performance

The most critical elements of the system that affect its performance are the PMTs. The network analyzer, the amplifier, and the rf switch all have a bandwidth of 500 MHz, while the PMTs have a bandwidth of 200 MHz. Another important factor is the rf shielding of the detection unit. The noise level can be reduced by proper shielding and grounding to yield greater signal-to-noise ratio (SNR). The noise level of the system was measured while the rf modulation signal for the lasers and the bias voltage for the PMTs (900 V) were kept applied, but no light is incident on the sample. The noise level was around −90 dBm up to 200 MHz, −80 dBm up to 250 MHz, −70 dBm up to 300 MHz, and −55 dBm up to 350 MHz. While the noise level increases with the modulation fre-
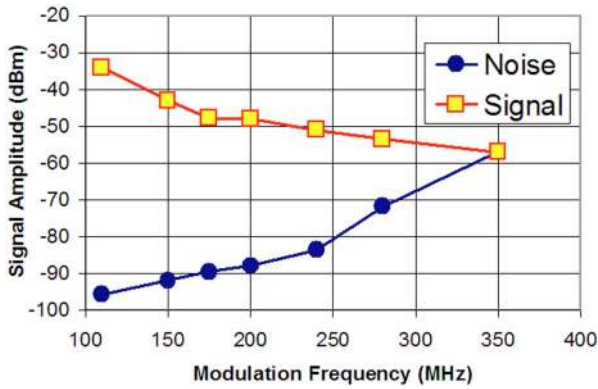
Fig. 5 The amplitude of the measured signal and noise with respect to modulation frequency.

quency, the signal decreases due to limited bandwidth of the PMT. To determine the useful bandwidth of the system, a homogeneous phantom was placed into the fiber optic interface, and the source-detector combination that provides the lowest signal was determined. Later, the modulation frequency was swept from 100 to 350 MHz for this source-detector combination. The bandwidth of the system is selected as the frequency at which the SNR drops below 30, and is determined as 300 MHz (Fig. 5). The minimum detectable signal at this frequency is −67 dBm, which corresponds to light power of 0.4 pW incident on the detector. The maximum modulation frequency in the phantom experiments was 280 MHz. Figure 6 shows the measured 64 amplitude values for the modulation frequencies of 110 and 280 MHz.

Measurement repeatability is also an important factor that affects performance of the imaging system. The DOT instrument and the lasers were turned on 30 min before the experiments to enable the system to warm up. To separate the errors arising from the fiber positioning and the instrument itself, repeatability tests were conducted with and without the repositioning of the homogeneous phantom.[23] First, the phantom was placed in the fiber optic interface and measurements were repeated ten times. The average rms errors in the amplitude and phase measurements were found to be 0.5% and 0.2 deg. The repeated measurements were also acquired for the case in which the phantom is removed and repositioned between each measurement. To eliminate the errors due to the inhomogene-
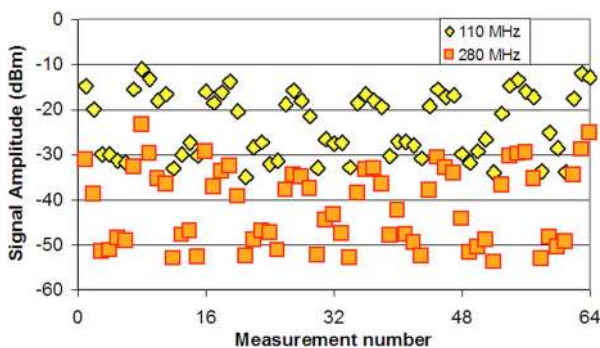

Fig. 6 The measured 64 amplitude values for the modulation frequencies of 110 and 280 MHz.

ity of the phantom, it was placed in the same orientation each time it was repositioned. In this case, the average rms error in the amplitude and phase measurements were found to be 4% and 0.4 deg. This error was caused only by the fiber probe repositioning. Later, the phantom was also rotated 45 deg between each measurement and the same error values were obtained. Therefore, it was concluded that the error due to the spatial variations of the phantom optical properties is less than the fiber repositioning errors. At the end of each experiment, a homogeneous phantom is placed in the fiber optic interface to acquire calibration data. The errors due to fiber repositioning would result in errors in the calibration and therefore affect the reconstructed image quality. These errors would cause fluctuations in the recovered optical properties in the imaging volume close to the source and detector probes, in addition to the inaccuracy in the recovered optical properties of the inclusion.

3.2 *Phantom Imaging*

For calibration purposes, a homogeneous phantom was used. A second phantom with a hole 15 mm in diameter was used to evaluate the performance of the system. The hole was positioned half the distance between the center and the edge. First, the concentration of the Intralipid and Indian ink was set to match the background optical properties of the solid phantom ($\mu_a=0.0132$ mm^{-1} and $\mu_{s'}=0.86$ mm^{-1}). Using this concentration as a reference, solutions with contrasts of 1.5:1, 2:1, and 2.5:1 in absorption coefficients are prepared. The data are acquired at 785 nm with six modulation frequencies, 110, 150, 175, 200, 240, and 280 MHz. After the calibration, the absorption and scattering maps were reconstructed using the inverse solver. First, six rows of Fig. 7 show the reconstructed absorption and scattering maps for the case with the contrast ratio of 2.5:1 at six different modulation frequencies. The seventh row shows the mean images obtained by averaging over six frequencies, while the last row shows the results obtained using multifrequency reconstruction. Figure 8 shows the mean of the reconstructed absorption values for all contrast cases in a region of interest (ROI) of 1 cm in diameter and the expected values. It is seen that the reconstructed absorption values increase with the modulation frequency and approach the expected value for all cases. On the other hand, the variations in the background region, which is homogeneous, increase as well. To take into account both of these effects, another metric for measuring the image quality, the contrast-to-noise ratio (CNR), was defined:[24]

$$\text{CNR} = \frac{\mu_{a,\text{ROI}} - \mu_{a,\text{back}}}{[(\omega_{\text{ROI}}\sigma_{\text{ROI}}^2 + \omega_{\text{back}}\sigma_{\text{back}}^2)]^{1/2}}/2, \qquad (1)$$

$$\omega_{\text{ROI}} = \text{area}_{\text{ROI}}/(\text{area}_{\text{ROI}} + \text{area}_{\text{back}}), \qquad (2)$$

$$\omega_{\text{back}} = \text{area}_{\text{back}}/(\text{area}_{\text{ROI}} + \text{area}_{\text{back}}), \qquad (3)$$

where $\mu_{a\text{ROI}}$ is the mean absorption coefficient for the ROI, $\mu_{a\text{back}}$ is the mean absorption coefficient for the background, σ_{ROI} is the standard deviation of the absorption distribution in the ROI, and σ_{back} is the standard deviation of the absorption distribution in the background. The coefficients
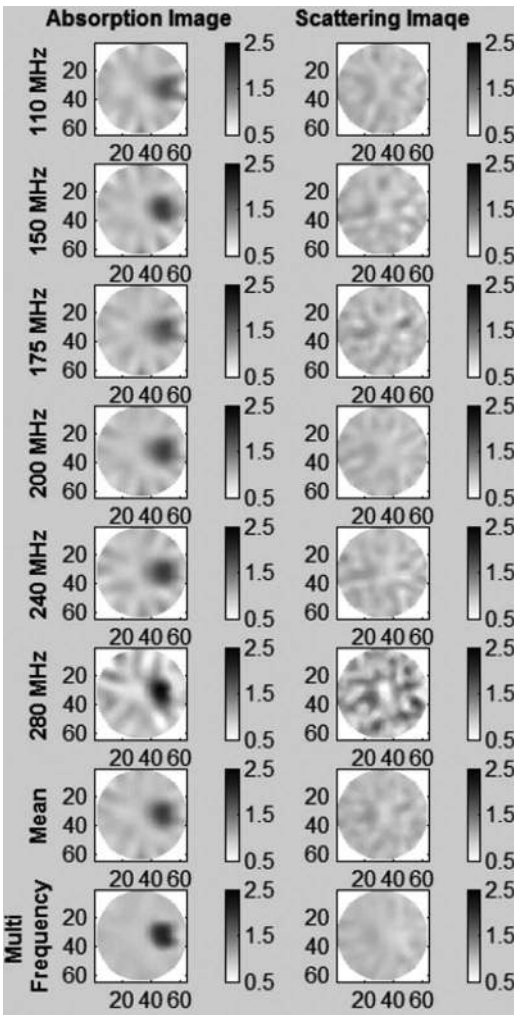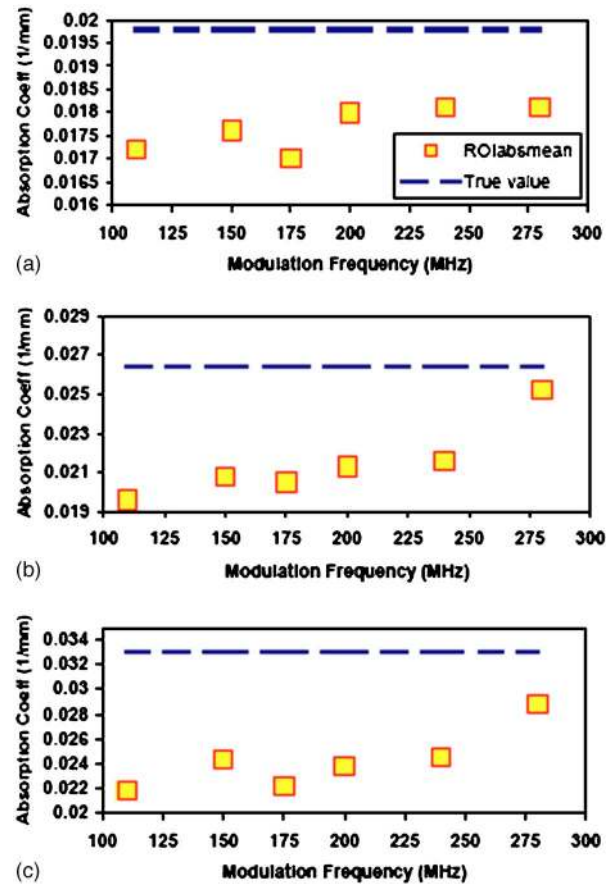
Fig. 7 First six rows show the reconstructed absorption and scattering maps for the case with the contrast ratio of 2.5:1 at six different modulation frequencies. The seventh row shows the mean image obtained by averaging over six frequencies, and the last row shows the results obtained using multifrequency reconstruction. The colormap was adjusted so that black and white colors correspond to 2.5 and 0.5 times the optical properties of the background, respectively.

Fig. 8 The mean of the reconstructed absorption values in a ROI of 1 cm in diameter for the contrast ratios of 1.5:1 (a), 2:1 (b), and 2.5:1 (c). The dotted lines show the expected values.

from 34% at 110 MHz down to 5% at 280 MHz. On the other hand, the fluctuations in the recovered optical properties in the background increase with the modulation frequency, as seen in Fig. 7. As a result, the related parameters Babsstd (stan-

ω_{ROI} and ω_{back} are introduced due to the area difference of the ROI and the background. The background region was defined as the whole area except for a 2.5-cm-diam circular region, as shown in Fig. 9.

A number of parameters were defined and used along with CNR for the evaluation of the image quality:
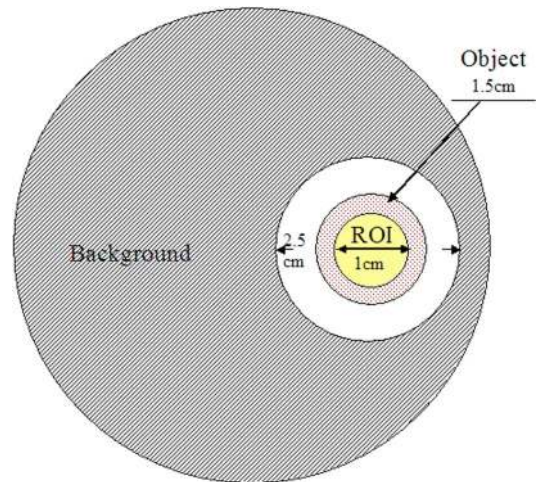- Full width at half maximum (FWHM): the average of the full width at half maximums on x axis and on $x = 16$ mm.
- ROIabsmean: mean absorption coefficient in the ROI.
- Babsstd: standard deviation of absorption coefficient distribution in the background.
- Bscamean: mean scattering coefficient in the background.
- Err: the percentage error calculated for the mean absorption coefficient in the ROI.

As seen in Table 2, the error in the recovered absorption coefficient reduces as the modulation frequency increases for all cases. For example, for the contrast case of 2.5:1, the error for the recovered absorption coefficient in the ROI reduces

Fig. 9 The object and the background regions selected for calculating the image quality related parameters.

Table 2 The values of the parameters used for evaluation of the image quality for the contrast ratio of 1.5:1, 2:1, and 2.5:1. The first six columns show the values of parameters for the reconstructed images at six different modulation frequencies. The seventh column shows the same parameters for the mean image obtained by averaging over six frequencies. The last column, on the other hand, shows the same parameters for multifrequency reconstruction.

Contrast ratio 1.5:1

								AVE	Multifrequency
Modulation Frequency	(MHz)	110	150	175	200	240	280		
FWHM	(mm)	16	15.5	15	16	16	11	14.5	13.5
ROIabsmax	(1/mm)	0.0181	0.0185	0.0183	0.0189	0.0188	0.0224	0.0187	0.020
ROIabsmean	(1/mm)	0.0172	0.0176	0.017	0.018	0.0181	0.0181	0.0177	0.0189
Babsstd	(1/mm)	0.0011	0.0009	0.0009	0.001	0.0011	0.0028	0.0008	0.0005
Bscamean	(1/mm)	0.87	0.86	0.86	0.86	0.87	0.95	0.888	0.86
CNR		5.6	7.2	6.3	7.1	7.0	2.7	7.9	16.3
Err	(%)	13	11	14	9	9	9	11	5

Contrast ratio 2:1

								AVE	Multifrequency
Modulation Frequency	(MHz)	110	150	175	200	240	280		
FWHM	(mm)	16	15	15.5	15.5	16	13.5	15	13.5
ROIabsmax	(1/mm)	0.0209	0.0221	0.0225	0.0231	0.023	0.0284	0.0233	0.0259
ROIabsmean	(1/mm)	0.0196	0.0208	0.0205	0.0213	0.0216	0.0252	0.0215	0.0228
Babsstd	(1/mm)	0.0013	0.0013	0.0012	0.0011	0.0013	0.0035	0.0011	0.0004
Bscamean	(1/mm)	0.87	0.86	0.87	0.86	0.86	1.04	0.89	0.86
CNR		7.1	8.8	9.1	10.8	9.7	5.3	11.1	19.5
Err	(%)	26	21	22	19	18	5	19	14

Contrast ratio 2.5:1

								AVE	Multifrequency
Modulation Frequency	(MHz)	110	150	175	200	240	280		
FWHM	(mm)	15	16	15.5	16	16	13.5	15	14.5
ROIabsmax	(1/mm)	0.0235	0.0261	0.0252	0.0258	0.0271	0.0342	0.0268	0.0297
ROIabsmean	(1/mm)	0.0218	0.0243	0.0222	0.0238	0.0245	0.0288	0.0243	0.0273
Babsstd	(1/mm)	0.0016	0.0014	0.0014	0.0012	0.0017	0.003	0.0012	0.0006
Bscamean	(1/mm)	0.87	0.86	0.87	0.86	0.86	0.94	0.88	0.86
CNR		8.1	11.5	9.3	12.4	10.1	7.0	13.2	25.2
Err	(%)	34	26	33	28	26	5	26	17

dard deviation of absorption coefficient distribution in the background) and Bscamean (the mean scattering coefficient in the background) increase as well.

These results show that evaluating the image quality only with error in the recovered optical parameters of the object would be misleading as expected, therefore the contrast ratio parameter (CNR) would help in assessing the image quality. As seen from Table 2, the CNR increases up to a certain modulation frequency and then starts decreasing. For cases with the contrast ratios of 2:1 and 2.5:1, the highest CNR was obtained at 200 MHz, while for the case with the smallest contrast ratio (1.5:1), the CNR obtained at 200 MHz was comparable to the one obtained at 150 MHz. The values in the seventh column of Table 2 show the values for the parameters obtained after averaging all of the images obtained at six different modulation frequencies (the mean image). Although

the CNR values for the mean image are higher than the values obtained at discrete modulation frequencies, the CNR for the multifrequency reconstruction result is the highest for all cases (last column in Table 2).

The full width at half maximums (FWHMs) obtained from the profiles in the x and y directions along the object were averaged to get a single parameter, FWHM. The FWHMs obtained from the profiles at discrete frequencies were similar, except smaller FMHMs along the x direction were observed at 280 MHz. It is believed to be due to the increased variations in the background.

4 Discussion

In this work, a novel multiwavelength and multifrequency imaging system is described. The system is computer con-

trolled and based on a network analyzer that allows utilization of multiple modulation frequencies. The performance of the system is evaluated with phantom studies. The bandwidth of the system and the minimum detectable power of the optical signal are determined to be 300 MHz and 0.4 pW, respectively. It should be noted that the modulation frequency could be increased at the expense of a higher minimum detectable signal. However, the measured signals in the animal and breast experiments could be as low as subpicowatt range and this is the reason behind our intention to report the bandwidth of the system for subpicowatt signal levels. The noise of the system has been measured as 0.5% in the amplitude and 0.2 deg in phase.

There are only a couple of studies reported with multiple modulation frequencies in the literature. Jiang et al. carried out experiments and simulations at mainly three different modulation frequencies, 50, 200, and 300 MHz.[25] In the simulation studies, they added noise up to 5% for both amplitude and phase shift. They did not observe any effect of the modulation frequency on the reconstructed image. O'Leary et al., however, observed a modulation-frequency-dependent improvement in image quality in systems with low background absorption (i.e., 0.01 cm^{-1} < μ_a < 0.1 cm^{-1}).[26]

In this study, it has been found that the image quality depends on the modulation frequency. The CNR improves with increasing modulation frequency up to 200 MHz; however, it starts degrading above that modulation frequency. This improvement hinges on the variation of the signal-to-noise ratio (SNR) in amplitude and phase with the modulation frequency. The dynamic amplitude and phase error of the network analyzer is almost constant between +10 and −50 dBm. As the modulation frequency increases, the signal amplitude decreases, and therefore the SNR in amplitude decreases. On the other hand, the measured phase shift increases with the modulation frequency, and this leads to an improved SNR in phase up to 200 MHz, where the signal amplitude is above −50 dBm. Above 200 MHz, the SNR in phase also decreases, and this explains the reduction in the image quality above 200 MHz. It should be noted that this optimum modulation frequency (200 MHz) is specific to our instrumentation and considerable effort is spent to increase the optimum modulation frequency further.

In addition to these, the reconstructed absorption and scattering maps obtained at six discrete frequencies were averaged and a mean image was obtained. The same analysis on this mean image revealed that the CNR values obtained after averaging are even higher than the values obtained at discrete modulation frequencies. Moreover, a multifrequency reconstruction approach was applied to the data, and single absorption and scattering images were obtained from the data obtained at six discrete frequencies. The analysis showed that the multifrequency reconstruction provides the superior image quality indicated by the lowest error and highest CNR values compared to the images obtained at optimum frequency (200 MHz), or even the mean image obtained by averaging the images acquired at discrete frequencies. Moreover, it is seen that the artifacts in the recovered absorption and scattering images close to the source and detector sites are reduced drastically.

Gao, Zhao, and Yamada reported improved image quality with the use of full time-resolved (TR) data.[27] The approximately linear relationship between the mean TOF in the time domain and the phase shift in the frequency domain was demonstrated. Based on this relationship, they concluded that their analysis in the time domain corresponds to the usage of multiple frequencies in the frequency domain, and the reconstruction quality would be substantially enhanced at different frequencies. Milstein et al. reported that multifrequency fluorescence diffuse optical tomography data do not provide useful information for single sphere inclusion but for some complex problems with higher resolution image components.[28]

The multifrequency approach reported in this manuscript has great potential to substantially increase the quality of the images obtained by diffuse optical tomography systems. A more thorough phantom study is currently being undertaken. In the ongoing studies, phantoms with higher contrast, different irregular-shaped compartments, and smaller inclusions are used to investigate the efficiency of a multifrequency approach in the reconstruction of higher contrasts and complex shapes.

Acknowledgments

References

1. J. P. Culver, R. Choe, M. J. Holboke, L. Zubkoy, T. Durduran, A. Slemp, V. Ntziachristos, B. Chance, and A. G. Yodh, "Three-dimensional diffuse optical tomography in the parallel plane transmission geometry: Evaluation of a hybrid frequency domain/continuous wave clinical system for breast imaging," *Med. Phys.* **30**(2), 235–247 (2003).
2. H. Dehghani, B. W. Pogue, S. P. Poplack, and K. D. Paulsen, "Multiwavelength three-dimensional near-infrared tomography of the breast: initial simulation, phantom, and clinical results," *Appl. Opt.* **42**(1), 135–145 (2003).
3. B. J. Tromberg, N. Shah, R. Lanning, A. Cerussi, J. Espinoza, T. Pham, L. Svaasand, and J. Butler, "Non-invasive in vivo characterization of breast tumors using photon migration spectroscopy," *Neoplasia* **2**(1,2), 26–40 (2000).
4. A. Li, Q. Zhang, J. P. Culver, E. L. Miller, and D. A. Boas, "Reconstructing chromophore concentration images directly by continuous-wave diffuse optical tomography," *Opt. Lett.* **29**(3), 256–258 (2004).
5. S. D. Jiang, B. W. Pogue, T. O. McBride, and K. D. Paulsen, "Quantitative analysis of near-infrared tomography: sensitivity to the tissue-simulating precalibration phantom," *J. Biomed. Opt.* **8**(2), 308–315 (2003).
6. T. O. McBride, B. W. Pogue, E. D. Gerety, S. B. Poplack, U. L. Osterberg, and K. D. Paulsen, "Spectroscopic diffuse optical tomography for the quantitative assessment of hemoglobin concentration and oxygen saturation in breast tissue," *Appl. Opt.* **38**(25), 5480–5490 (1999).
7. D. A. Boas, T. Gaudette, G. Strangman, X. Cheng, J. Marota, and B. J. Mandeville, "The accuracy of near infrared spectroscopy and imaging during focal changes in cerebral hemodynamics,"*Neuroimage* **13**, 76–90 (2001).
8. A. Bluestone, G. Abdoulaev, R. Barbour, C. Schmitz, and A. H. Hielscher, "Three-dimensional optical-tomographic localization of changes in absorption coefficients in the human brain," *Proc. SPIE* **4250**, 258–268 (2001).
9. D. Grosenick, H. Wabnitz, H. H. Rinneberg, K. T. Moesta, and P. M. Schlag, "Development of a time domain optical mammography and

first in vivo applications," *Appl. Opt.* **38**, 2927–2943 (1999).
10. V. Ntziachristos and B. Chance, "Breast imaging technology: Probing physiology and molecular function using optical imaging-applications to breast cancer," *Breast Cancer Res.* **3**(1), 41–46 (2001).
11. A. E. Cerussi, D. Jakubowski, N. Shah, F. Bevilacqua, R. Lanning, A. J. Berge, D. Hsiang, J. Butler, R. F. Holcombe, and B. J. Tromberg, "Spectroscopy enhances the information content of optical mammography," *J. Biomed. Opt.* **7**(1), 60–71 (2002).
12. B. Chance, M. Cope, E. Gratton, N. Ramanujam, and B. Tromberg, "Phase measurement of light absorption and scatter in human tissue," *Rev. Sci. Instrum.* **69**(10), 3457–3481 (1998).
13. M. Gurfinkel, T. Pan, and E. M. Sevick-Muraca, "Determination of optical properties of semi-infinite turbid media using area measurements of frequency-domain photon migration obtained with an ICCD system," *J. Biomed. Opt.* **9**(6), 1336–1346 (2004).
14. S. Fantini, M. A. Franceschini, G. Gaida, E. Gratton, H. Jess, W. W. Mantulin, K. T. Moesta, P. M. Schlag, and M. Kaschke, "Frequency-domain optical mammography: edge effect corrections," *Med. Phys.* **23**, 149–157 (1996).
15. T. O. McBride, B. W. Pogue, S. Jiang, U. L. Österberg, and K. D. Paulsen, "A parallel-detection frequency-domain near-infrared tomography system for hemoglobin imaging of the breast in vivo," *Rev. Sci. Instrum.* **72**, 1817–1824 (2001).
16. X. Intes, C. Maloux, M. Guven, B. Yazici, and B. Chance, "Diffuse optical tomography with physiological and spatial a priori constraints," *Phys. Med. Biol.* **49**(12), N155–163 (2004).
17. M. Firbank, M. Oda, and D. T. Delpy, "An improved design for a stable and reproducible phantom material use in near infrared spectroscopy and imaging," *Phys. Med. Biol.* **40**, 955–961 (1995).
18. B. C. Wilson and M. S. Patterson, "Future directions and applications in photodynamic therapy," *Proc. SPIE* **1506**, 219–231 (1990).
19. F. E. W. Schmidt, M. E. Fry, E. M. C. Hillman, J. C. Hebden, and D. T. Delpy, "A 32-channel time-resolved instrument for medical optical tomography," *Rev. Sci. Instrum.* **71**, 256 (2000).
20. T. O. McBride, B. W. Pogue, U. L. Österberg, and K. D. Paulsen, "Strategies for absolute calibration of near infrared tomographic tissue imaging," *Adv. Exp. Med. Biol.* **531**, 85–100 (2003).
21. S. R. Arridge and J. C. Hebden, "Optical imaging in medicine: II. Modelling and reconstruction," *Phys. Med. Biol.* **42**, 841–853 (1997).
22. P. C. Hansen and D. P. O'Leary, "The use of the L-curve in the regularization of discrete ill-posed problems," *SIAM J. Sci. Comput. (USA)* **14**(6), 1487–1503 (1993).
23. J. J. Stott, J. P. Culver, S. R. Arridge, and D. A. Boas, "Optode positional calibration in diffuse optical tomography," *Appl. Opt.* **42**(16), 3154–3162 (2003).
24. X. Song, B. W. Pogue, S. Jiang, M. M. Doyley, H. Dehghani, T. D. Tosteson, and K. D. Paulsen, "Automated region detection based on the contrast-to-noise ratio in near infrared tomography," *Appl. Opt.* **43**, 1053 (2004).
25. H. Jiang, K. D. Paulsen, U. L. Osterberg, B. W. Pogue, and M. S. Patterson, "Optical image reconstruction using frequency-domain data: simulations and experiments," *J. Opt. Soc. Am. A* **13**, 253–266 (1996).
26. M. A. O'Leary, D. A. Boas, B. Chance, and A. G. Yodh, "Experimental images of heterogeneous turbid media by frequency-domain diffusing-photon tomography," *Opt. Lett.* **20**(5), 426–428 (1995).
27. F. Gao, H. J. Zhao, and Y. Yamada, "Improvement of image quality in diffuse optical tomography by use of full time-resolved data," *Appl. Opt.* **41**, 778–791 (2002).
28. A. B. Milstein, J. J. Stott, O. Seungseok, D. A. Boas, R. P. Millane, C. A. Bouman, and K. J. Webb, "Fluorescence optical diffusion tomography using multi-frequency data," *J. Opt. Soc. Am. A* **21**(6), 1035–1049 (2004).